Efficient Aqueous Electroreduction of CO_2 to Formate at Low Overpotential on Indium Tin Oxide Nanocrystals

Huei-Ru "Molly" Jhong [a§], Uzoma O. Nwabara[b§], Sofia Shubert-Zuleta[c], Nicholas S. Grundish[d], Bharat Tandon[a], Lauren C. Reimnitz[a], Corey M. Staller[a], Gary K. Ong[a], Camila A. Saez Cabezas[a], John B. Goodenough[d], Paul J.A. Kenis*[b], and Delia J. Milliron*[a]

a. *McKetta Department of Chemical Engineering, University of Texas at Austin, Austin, Texas 78712, United States*
b. *Departments of Chemical & Biomolecular Engineering, University of Illinois at Urbana-Champaign, 600 South Mathews Avenue, Urbana, Illinois 61801, United States.*
c. *Department of Chemistry, University of Texas at Austin, Austin, Texas 78712, United States.*
d. *Materials Science and Engineering Program and Texas Materials Institute, The University of Texas at Austin, Austin, Texas 78712, United States*

[§]These authors contributed equally.

*Authors to whom correspondence should be addressed. Email: milliron@che.utexas.edu; kenis@illinois.edu

Abstract

Electroreduction of CO_2 to formate powered by renewable energy offers an alternative pathway to producing carbon fuels that are traditionally manufactured using fossil fuels. However, achieving simultaneously high partial current density (j_{HCOO^-}), high product selectivity (Faradaic efficiency (FE_{HCOO^-})), and low overpotentials (η) remains difficult due to the lack of suitable catalysts. Here, we report the electroreduction of CO_2 on Sn-doped indium oxide (ITO) nanocrystal catalysts in an alkaline flow electrolyzer. Colloidally synthesized monodisperse 20 nm ITO NCs with various Sn doping levels (0, 1, 5, 6.5, 8, and 12 atomic%) were studied. We find that ITO NC catalysts exhibit a high selectivity

for production of $HCOO^-$ over CO and H_2 (approximately 87% $HCOO^-$, 1-4% CO, and 2-6% H_2 at -0.85 V vs. RHE), an onset potential for $HCOO^-$ as early as -0.21 V vs. RHE, as well as a high partial current density for $HCOO^-$ up to 171 mA/cm^2 at a cathode potential of -1.08 V vs. RHE. The main difference between the catalysts' performances resides in the onset potential for formate production. Onset of formate production occurred at cell and cathode overpotentials of only –440 mV and –143 mV, respectively, by the 12% ITO. Analysis of the ITO electrodes before and after electrolysis suggest no changes in surface composition, crystal structure, or particle size occur under the reduction conditions. Tafel slopes of ITO NC catalysts range from 27 to 52 mV per decade, suggesting the rate determining step is likely the proton-coupled electron transfer to $CO_2^{\bullet -*}$ to form $HCOO^{-*}$.

Introduction

Present, and still rising, carbon dioxide (CO_2) levels in the atmosphere have been linked to climate change, necessitating multifaceted approaches to curb further undesired effects. Multiple approaches, such as carbon sequestration, electrification of the transportation sector, and switching from fossil fuels to renewable sources, will need to be implemented to curb the increase in CO_2 levels.[1, 2] Addressing the main challenge of implementing renewable sources[i] such as wind and solar, their intermittency, will require development of a scalable and broadly deployable means for storage of electricity. Electrochemical reduction of CO_2 into carbon-based fuels and chemicals has been widely proposed for the storage and utilization of intermittent renewable sources.[3-5] While research over the past few decades has shown that the CO_2 electroreduction reaction (CO_2RR) can occur on various metals and produce a host of products, current catalysts do not exhibit sufficient activity (*i.e.*, current density), selectivity (*i.e.*, Faradaic efficiency (FE)), and energetic efficiency (related to overpotential) for this application.[4]

Formate is a key chemical for many industries.[6] Heavy post-transition metals such as indium and tin have been identified as promising catalysts for selectively producing formate, with small amounts of carbon monoxide (CO) and hydrogen (H_2). Various research labs have conducted studies comparing the performance of indium oxides and tin oxides to their metallic forms for CO_2 electroreduction to formate.[7-17] In fact, many of the best-performing catalysts do not solely consist of metallic Sn^0 or In^0; oxide-based materials are often superior.[4] For example, both Kanan *et al*. and Broekmann *et al*. have found that the

hydrogen evolution reaction (HER) dominated on oxide-stripped Sn^0 while formate was selective on SnO_x.[11, 12] While significant efforts have focused on indium, tin, and their oxide forms for CO_2 electroreduction, fewer reports have focused on the study of tin-doped indium oxide (ITO) nanocrystals (NCs). The use of colloidal synthesis to systematically control the size and composition of doped metal oxide nanocrystals such as ITO (*i.e.*, $Sn:In_2O_3$) NCs is now well established,[18] which enables us to examine the influence of dopant concentration on catalysis, while keeping NC size constant.

In this study, we synthesized monodisperse, homogeneously-doped ITO NCs (20 nm in size) with various Sn doping levels (0, 1, 5, 6.5, 8, and 12 atomic%) and investigate their catalytic activity for CO_2RR using a previously reported alkaline flow electrolyzer.[5, 19, 20] A potassium hydroxide (KOH) base ligand exchange method was reported, for the first time, to remove the bulky, native organic ligands from the NC surface to make it accessible for catalysis. XPS and XRD were performed on ITO NC catalysts before and after CO_2 electrolysis to study whether electrolysis affects the surface composition, crystal structure, and particle size of the ITO NCs. Tafel slope analysis was conducted to understand better the reaction kinetics of CO_2RR on ITO NCs.

Experimental Methods

Synthesis of ITO Nanocrystals

ITO NCs were synthesized by our previously reported method[21], which is a modification of methods

published by the Hutchison group.[22, 23] NCs were synthesized by adding 4.7 mmol of metal precursor (In(III) acetate and Sn(IV) acetate in the desired atomic ratio) to 10 mL of oleic acid in a round bottom flask. This flask will be referred to as the precursor flask. The precursor flask is then put under vacuum and heated to 110°C for 1 hour with one nitrogen purge midway through the hour. The precursor flask is then put under nitrogen and heated to 150°C for 2 hours to generate In- and Sn-oleate. Concurrently, 12 mL of oleyl alcohol is put in a second round bottom flask, called the reaction flask. The reaction flask is held under dynamic vacuum and heated to 150°C for 2 hours with one nitrogen purge midway through. The reaction flask is then heated to 290°C under nitrogen. The prepared In- and Sn-oleate precursor is pulled from the flask into a syringe for slow injection into the reaction flask by using a syringe pump. The injection rate is set to 0.2 mL/min and the total injection volume is 10 mL for 20 nm NC size. Following the injection the reaction flask is held at 290°C for 20 min before being cooled to room temperature. NCs are washed by 5 cycles of flocculating NCs with ethanol, centrifuging at 7500 RPM, and redispersing in hexane. The overall NC size and size polydispersity were measured by scanning transmission electron microscopy (STEM) and verified by dynamic light scattering (DLS) and X-ray diffraction (XRD). Overall Sn dopant incorporation was quantified by elemental analysis using inductively coupled plasma-atomic emission spectroscopy (ICP-AES) of acid-digested NCs.

KOH Ligand exchange method

To remove the native oleate ligand from the ITO NC surfaces, 10 mL of 0.1 M KOH in ultrapure Milli-Q water was added to a vial and 10 mL of 2.5 mg/mL ITO NC in hexane solution was deposited on top. The ligand exchange occurred over the next 24 hours and was noticeable where the water phase had a slight blue tint to it. During the exchange process, care was taken to not disturb the solution, as this causes irreversible emulsification. After the 24 hour period had passed, the aqueous layer was separated from the organic hexane layer. In the case of NCs caught at the liquid phase interface, gentle tapping of the vial allowed NCs to fall into the aqueous layer. Following, the excess KOH in the aqueous solution was washed by spin dialysis. The 10 mL of ITO/NCs in water was added to a centrifuge tube equipped with a spin dialysis filter (Amicon Ultra 2 mL centrifugal filters) and centrifuged at 4500 RPM for 5 minutes. The excess water was discarded and the remaining concentrated NC solution was diluted with 10 mL of ultrapure Milli-Q water; the spin dialysis tube was centrifuged again at 4500 RPM for 10 minutes. This process was repeated at least two more times, until the solution had reached a neutral pH. The final concentrated NC solution was diluted with 2 mL of ultrapure Milli-Q water.

Characterization of ITO Nanocrystals

STEM was performed with a Hitachi S5500 SEM/STEM instrument in bright-field mode at a 30 kV accelerating voltage. Ligand-capped samples were prepared for imaging by drop casting dilute dispersions of ITO NCs in hexane onto ultrathin carbon copper TEM grids and allowing the hexane to evaporate. Ligand-stripped samples were prepared the same way, except the TEM grids were heated

gently after drop casting to evaporate the water. NC diameter was determined by analyzing STEM images with ImageJ software, based on a minimum of 200 NCs.

ICP-AEM (Varian 720-ES ICP Optical Emission Spectrometer) measurements were conducted to characterize the overall tin dopant concentration of the ITO NCs after digesting the NCs with aqua regia.

XPS was collected with a Kratos Axis Ultra DLD spectrometer with a monochromatic Al Kα source (1486.6 eV). Resulting spectra were analyzed with CasaXPS equipped with the Kratos library of elemental relative sensitivity factors. Spectra were treated with a simple constant correction to calibrate the main carbon 1s peak to an energy of 284.8 eV.

DLS and Zeta potential measurements of both ligand-stripped and ligand-capped NC samples were conducted in a Malvern Zeta Sizer Nano ZS. Ligand-capped ITO NCs in hexane were diluted to approximately 1 mg/mL and filtered through a polytetrafluoroethylene membrane (0.45 μm pore size, PALL). The solution was then measured in an immersed dip cell (ZEN1002 Malvern). Ligand stripped ITO NCs in water were also diluted to approximately 1 mg/mL and filtered through a polyvinylidene fluoride membrane (0.45 μm pore size, PALL). The aqueous solutions were measured in a folded capillary cell (DTS1070 Malvern).

FTIR spectroscopy was carried out on a Bruker Vertex 70 spectrometer in transmission geometry with an average of 120 scans at 4 cm^{-1} resolution. All measurements were performed on undoped, double side polished silicon substrates cleaned by sonicating for at least 30 minutes in hexane, acetone, then

isopropanol. A clean Si substrate was used for background subtraction. Films of ligand-capped ITO NCs were prepared by spin coating and depositing 50 μL of 20 mg/mL ITO NCs dispersed in hexane. Films of ligand-stripped ITO NCs were prepared by spin coating on UV-ozone-treated Si substrates and depositing 50 μL of 20 mg/mL ITO NCs dispersed in water and ethanol (v/v=1/1).

XRD patterns were obtained on a Rigaku R-Axis Spider using Cu Kα radiation (1.54 Å). Colloidal ITO NCs in hexane (ligand-capped) or water (ligand-stripped) were precipitated with an antisolvent, ethanol or hexane, respectively, and centrifuged at 7500 rpm for 5 minutes. The resulting pellet was dried under vacuum for 24 hours. Samples were mounted on a cryoloop with mineral oil for measurement. Diffraction patterns of ITO NCs on gas diffusion electrodes (GDEs) were measured with the same instrumentation. The electrodes were cut down to approximately 2 mm x 2mm squares and mounted onto the same cryoloop with a small amount of mineral oil.

Electrochemical testing of ITO catalysts

Electrode Preparation for the Alkaline Flow Cell

The synthesized NCs and IrO_2 were deposited onto a carbon paper gas diffusion layer (GDL) to create the cathodes and anodes, respectively, *via* an airbrushing method reported previously.[24] For each Sn dopant concentration, ~4 mg of NCs dispersed in water were added to a glass vial along with 10.5 μL of Nafion (5 wt%, Fuel Cell Earth) and an additional 1 mL of DI water. When airbrushing the ligand-capped NCs, dispersed in hexane, hexane was used in place of DI water. The resulting ink was then

airbrushed onto a 2.5 cm x 0.8 cm GDL (Sigracet 35 BC, Fuel Cell Store), representing 1 cathode, to obtain a final loading of 1.0 ± 0.1 mg cm^{-2}. For the anode, ~20 mg of commercial IrO_2 (non-hydrate, Alpha Aesar) were combined with 52 μL of Nafion, 500 μL of DI water, and 1 mL of IPA then sonicated in a water bath for 20 min to obtain a homogeneous ink, which was then airbrushed onto a 5.0cm x 2cm GDL, representing 4 anodes, to obtain a final loading of 1.0 ± 0.1 mg cm^{-2}. A fresh electrode was used for each experiment.

Alkaline Flow Electrolyzer operation

Electrochemical CO_2 reduction was carried out in a custom-made GDE-based alkaline flow electrolyzer.[5, 19] Stainless steel (SS) plates served as current collectors to hold the flow cell together *via* a squeeze-action toggle plier clamp (McMaster Carr). The SS plates provided electrical contact between the GDEs and a method for connecting the cell to the potentiostat (Autolab PGSTAT-30) used to apply various cell potentials. CO_2 was flowed to the cathode gas compartment via a flow meter (Cole-Parmer) at 17 SCCM. A syringe pump (Harvard Apparatus PHD 2000) flowed 1 M KOH, used for both the catholyte and the anolyte, at 0.5 mL min^{-1} to the polyether ether ketone (PEEK) electrolyte chambers, which were separated by an anion exchange membrane (PK-75, Fumatech). For each electrolysis experiment, the potentiostat was used to apply cell potentials of –1.75 V, –2.00 V, –2.25 V, –2.50 V, –2.75 V, –3.00 V, and –3.50 V and record the resulting total current. Multimeters (Crenova, MS8233D) measured the corresponding cathode and anode potentials against a Ag/AgCl reference electrode (Basi,

RE-5B). Products of the reduction were analyzed to determine the activity (partial current density) and the Faradaic efficiency of the catalyst. The gaseous product stream was fed directly to a gas chromatograph (Thermo Finnigan Trace GC) furnished with a thermal conductivity detector. Liquid product samples were collected from the electrolyte and later prepared and analyzed with NMR (Agilent VNS 750NB). The alkaline flow electrolyzer experiments were conducted 3 separate times for each Sn dopant concentration, each with freshly airbrushed undoped In_2O_3 or ITO cathodes and IrO_2 anodes.

Results and Discussion

In this study, we investigate the Sn doping series (0, 1, 5, 6.5, 8, and 12 at%) of ITO NCs for electroreduction of CO_2 to formate and CO. The Sn dopant series of the monodisperse 20 nm size ITO NCs was synthesized using a standard Schlenk line setup by the slow growth synthesis method reported by the Hutchison group, which is a well-developed colloidal synthesis protocol that allows for precise size and dopant control for doped metal oxide nanocrystals. Note that 12 at% Sn is the synthetic doping limit of ITO NCs. ITO NCs with pseudospherical morphology were observed (**Figure 1** top-right and **Figure S1**). The 3D tomographic virtual model, obtained from X-ray micro-computed tomography (MicroCT), of the gas diffusion electrode (GDE) characterizes a uniform catalyst layer of ITO NCs (5% ITO in **Figure 1** top-left) with catalyst layer thickness of approximately 16 μm.[24] A previously-published dual

electrolyte channel flow electrolyzer was employed to characterize the electrochemical performance of ITO NCs (**Figure 1** bottom panel).[20]

Doped metal oxide NCs such as ITO are typically synthesized in a solution containing surface ligands, which post-synthetically remain on the NCs with an anchoring headgroup tethered to the NC surface and a hydrocarbon tail directed away from it.[25, 26] Interaction between the NC and ligand headgroup is used to classify the types of ligands (L-, X-, and Z-types). X-type ligands are commonly monovalent ions binding oppositely charged sites at the NC surface. Examples of X-type ligands include carboxylates ($RCOO^-$), thiolates (RS^-), as well as inorganic ions such as Cl^- and OH^-. Surface ligands consisting of an X-type headgroup and a hydrocarbon tail allow (i) control over the kinetics of NC nucleation and growth and (ii) the NCs to colloidally disperse in nonpolar, hydrophobic solvents such as hexane. The colloidally synthesized ITO NCs in this study are capped with oleate (OA), which is an X-type ligand, and are dispersed in hexane. However, the presence of such bulky capping molecules creates a hydrophobic steric barrier around each NC. Especially in an aqueous environment, this steric barrier may block the access of reactant molecules to the NC surface or may hinder the removal of product molecules from the NC surface, which is disadvantageous for catalytic applications.[27] Moreover, catalyst inks for electrocatalysis are typically prepared using dispersion of nanoparticles in water and in isopropyl alcohol. Therefore, ligand exchange is necessary to remove the bulky ligands from the NC surface and to transfer NCs from hexane to water. To address the issue, we developed a KOH ligand

exchange method. The KOH ligand exchange was carried out by using 10 mL of 2.5 mg/mL ITO in hexane slowly added in to a vial containing 10 mL of 0.1 M KOH aqueous solution. After reacting for 24 hours, the oleate ligands were replaced by hydroxyl (OH^-) ligands, resulting in NC transfer to the water phase. Subsequent purification yields a water dispersion of ITO NCs with neutral pH. We chose KOH based on a hypothesis that hydroxyl can also act as an X-type ligand; thereby exchange with oleate is possible without violating charge neutrality of the NCs. **Figure 2** shows the characterization of the KOH ligand exchange method on a representative sample, 20 nm 5 % ITO NCs. STEM images of the ITO NCs before and after KOH treatment, respectively, revealed that the NC shape and size are preserved (**Figure 2a and b**). Sizing of the NCs before and after ligand exchange show nearly identical average particle size (20.2 ±1.4 nm for particle count of 200) (**Figure S2**). The aggregate-free nature of the NC dispersion is verified by the monomodal size distributions measured by dynamic light scattering (DLS) (**Figure 2c**). The hydrodynamic diameters of ligand-capped and –stripped ITO NCs are 24.4 nm and 21.0 nm, respectively. The slightly larger hydrodynamic diameter of ligand-capped NCs may be attributed to the capping layer of OA ligands around each NC. Zeta potentials of the ligand-capped and –stripped ITO NCs are +0.3 mV and -38.9 mV, respectively. The nearly zero zeta potential of the ligand-capped NCs is consistent with a sterically stabilized colloidal dispersion, made possible by the long hydrocarbon chains of the OA ligands.[27] The surface of ligand-stripped ITO NCs are negatively charged (ζ = -38.9 mV) for a pH 7 dispersion because the isoelectric point of the ITO NCs is around pH 4-5

(**Figure S3**). A zeta potential with magnitude of at least 25 mV is typical for electrostatic charge stabilization of a NC dispersion. The doping series of ITO NCs all exhibit zeta potentials between -35 to -75 mV. XRD patterns of ligand-capped (blue) and ligand-stripped (red) ITO NCs reveal the standard bixbyite crystal structure for ITO NCs (**Figure 2e**), which is in good agreement with the In_2O_3 bixbyite reference pattern (PDF #00-006-0416) included at the bottom. The four most intense XRD peaks of ITO NCs are indexed. Scherrer analysis results for two of the most intense In_2O_3 diffraction peaks at 30.6 and 35.5 degrees 2Θ suggest the crystallite sizes are similar before and after ligand exchange (**Table S1**). Fourier transform infrared spectroscopy (FTIR) is a reliable way to probe the NC surface. The native OA ligands have long chain hydrocarbons giving rise to a strong C-H stretch in the infrared around 3,000 cm^{-1}(**Figure 2f**). The C-H stretch infrared absorption is observed to shrink significantly after ligand stripping, but is not eliminated completely. We observed similar characterization results on the undoped In_2O_3 NCs before and after KOH ligand exchange (**Figure S4**). All the ITO NCs were ligand stripped using the KOH ligand exchange method prior to electrochemical measurements unless otherwise specified.

We measured the electrochemically active surface area (ECSA) of a few ITO samples (0, 1, and 5% ITO) via the double layer capacitance (DLC) method to confirm that a minimal particle size effect on catalytic activity is anticipated for the Sn doping series of ITO NCs, consistent with their sizes being similar, all close to 20 nm. DLC method is one of the most reliable methods for measuring the ECSAs of metal oxides.[15, 28-30] In Ar-saturated electrolyte (0.15 M $NaClO_{4\,(aq)}$), cyclic voltammograms (CVs) at

various scan rates (5, 10, 20, 30, 40, and 50 mV/s) were recorded for 0.1 mg ITO NCs deposited on a glassy carbon disk electrode (0.196 cm^2) over a narrow potential range, ±50 mV centered on the open circuit potential (OCP), where there is no Faradaic current response, using a standard 3-electrode electrochemical cell. In the middle of the potential window, the double layer capacitive current (i_c) was taken as the average of the anodic and cathodic currents. The i_c was plotted against the scan rate, and i_c follows the expected linear behavior of an ideal capacitor with scan rate, given by $i_c = \nu C_{DL}$.[29] The slope of this straight line is electrode capacitance (μF), C_{DL}, which is converted to ECSA ($m^2\ g^{-1}$) via a specific capacitance of 10 μF cm_{oxide}^{-2}.[15, 28-30] **Figure S5** shows that the Sn doping series of ITO NCs exhibit similar slopes (8.3 ± 0.8 μF), which correspond to ECSA of about 1 $m^2\ g^{-1}$ (in good agreement with prior studies on metal oxides).[15, 28] Similar ECSAs measured by DLC among the doping series of ITO NCs suggest that a particle size effect can likely be neglected as we anticipated, and as a result, their intrinsic electrocatalytic activity may be evaluated.

The Sn doping series of ITO NC catalysts immobilized on GDE were tested in a flow electrolyzer. The total current densities of the flow electrolyzer and the individual electrode (cathode and anode) polarization curves are shown in **Figure 3**. Specifically, in **Figure 3a** we see that introducing Sn to indium oxide results in a higher total current density. The undoped In_2O_3 reached current densities just under 200 mA cm^{-2} at –3.50 V of cell potential. The doped ITO NCs begin to outperform the undoped In_2O_3 around –2.75 V and reach current densities between 225 and 260 mA cm^{-2} at –3.50 V of cell potential.

Our results for and comparison of each catalyst were reproducible over all 3 replicates conducted. These results reveal that adding even a small amount of Sn enhances the performance of In_2O_3 for CO_2 electroreduction. Unsurprisingly, the ligand-capped 5% ITO NCs exhibited the lowest current densities most likely due to blocking of active sites by the ligands. However, we note that despite omitting the stripping step for this particular sample, the ligand-capped NCs are still active for CO_2 electroreduction to $HCOO^-$, though exhibiting a significantly lower activity than the ligand-stripped sample. This activity may be due to the fact we use KOH as our electrolyte, which is the same salt used to strip the ligands during post-synthetic treatment. Some of the ligands at the surface of the catalyst layer may have therefore been stripped during electrolysis, allowing for CO_2 electroreduction activity. White *et al.* came to similar conclusions, attributing the slightly enhanced activity of the ligand-stripped In nanoparticles to removal of ligands (*i.e.*, oleylamine in their study).[9] The individual electrode polarization curve (**Figure 3b**) reveals a consistent performance by the anode across all experiments, which gives more confidence to the comparisons made between the various cathode catalysts.

The partial current densities and Faradaic efficiencies of ITO electrodes as a function of potential is depicted in **Figure 4**. Only $HCOO^-$, carbon monoxide (CO), and hydrogen (H_2) were detected from the ITO electrodes. Note that a trace amount of acetate was detected in NMR (**Figure S6**). A $HCOO^-$ partial current density of 171 mA cm^{-2} was achieved by the 6.5% ITO catalyst at –1.08 V vs RHE. Again, the 5% ligand-capped catalyst expressed the lowest performance, reiterating that the ligands block active

sites for formate production thus allowing HER to proceed (**Figure 4e** and **4f**). When comparing across the various ligand-stripped NC catalysts (**Figure 4a**), however, we see that the partial current density of $HCOO^-$ does not greatly depend on the Sn at. %. Moreover, **Figure 4b** depicts that the $HCOO^-$ Faradaic efficiency for all tested catalysts, including undoped In_2O_3 and the 5% ligand-capped, reached values of at least 80%, with the 8% ITO and 12% ITO catalysts reaching 87% Faradaic efficiency at -0.85 and -0.63 V vs. RHE, respectively. Again, we saw similar results for our catalysts across multiple experiments with different catalyst batches. We note that the observed FEs might be affected by loss of CO_2 to the electrolyte and/or carbonate formation, issues that are being pursued in dedicated studies by us and others.[31-35] The main difference between the catalysts' performances resides in the onset potential for formate production. All of the Sn-doped, ligand-stripped catalysts reveal that introducing Sn permits formate production at lower cathode potentials, specifically ≥ –0.30 V vs RHE (cathode overpotential $\eta_{cathode} \leq 233$ mV as the standard electrode potential for CO_2RR to formate (E^o) is –0.067 V vs. RHE[36]). This can also be interpreted in terms of lower cell potentials, ≥ –1.75 V (cell overpotential $\eta_{cell} = \leq 440$ mV as $E^o_{cell} = E^o_{cathode} - E^o_{anode} = (-0.067\ V\ vs.RHE) - (1.23\ V\ vs.RHE) = -1.297\ V)$. Cathode overpotentials provide insight in understanding the kinetics of electrode reactions, whereas cell overpotentials are useful as these determine the energetic efficiency of the reactor, which is a key performance benchmark for evaluating the technoeconomic feasibility of CO_2RR.[37] The undoped In_2O_3 and 5% ligand-capped catalyst begin to produce formate at a cell potential of –2.00 V ($\eta_{cell} \geq 700$ mV).

The catalyst with the highest Sn-doping level, 12% ITO, exhibited the lowest onset potential of –0.21 V vs RHE for formate formation ($\eta_{cathode}$ = 143 mV), 260 mV lower than that of the undoped In_2O_3 catalyst. The ITO NCs exhibited onset overpotentials lower (more positive) than those reported for Sn- or In-based catalysts for CO_2RR to HCOOH/$HCOO^-$.[7, 9-11] Specifically, Liu *et al.* reported a comparative onset overpotential (–0.4 V vs. RHE, $\eta_{cathode} \leq$ 200 mV) by studying In_2O_3@$C_{11.6\%}$, but the highest observed $HCOO^-$ current density for this catalyst was 14.8 mA cm^{-2} while we report 171 mA cm^{-2}.[15] Interestingly, moderate Faradaic efficiency for formate formation (~50%) was obtained even at such low onset potential of -0.21 V vs. RHE for the 12% ITO. In addition, the 12% ITO catalyst was most selective toward formate over H_2 as it reached ~80% Faradaic efficiency at –0.36 V vs RHE, which is about 40 mV lower than that for the other ligand-stripped ITO catalysts. There is also a notable increase in acetate production with the 12% ITO compared to all other catalysts tested (**Figure S6**). Although the exact mechanism for acetate formation from CO_2 electrocution is still debated, the two commonly proposed reaction pathways are through carbon dimerization or carbon insertion, both of which involve CO* as a key intermediate.[38] Therefore, the higher amount of Sn in the 12% ITO catalyst may also help to stabilize CO* for acetate formation to a point. Too strong of a bond of CO to the active site may result in catalyst poisoning, which would lower CO_2RR activity and discourage carbon coupling.[39] From these results collectively, we understand that the addition of Sn helps to stabilize the intermediates in the $HCOO^-$ reaction mechanism.

From our results we suggest that with Sn doping, the ITO catalysts possess SnO_x surface species that lower onset potentials and reduce the energy requirement for the reaction. In fact, increasing the SnO_2 concentration improved the electrical conductivity of ITO nanocrystals to a certain point.[40] Previous studies have shown In oxides ($In_2(OH)_3$ and In_2O_3) alone compared to In^0 were more stable in operating conditions, and an In-OH layer covering the electrode surface aided in suppressing the hydrogen evolution reaction (HER).[7, 9] In addition, a DFT study by Xin *et al.* indicated that oxygen vacancies on certain facets of SnO_x catalysts adsorbed and stabilized CO_2, thus lowering the energy barrier for formate production.[8] Specifically, the oxygen vacancies favored the formation of CO_2^* while embedded hydroxyls (–(O)H*) favored HCO_3^*, thus leading to higher formate activity through a lower energy pathway. Amal *et al.* came to similar conclusions, attributing their relatively low onset potential (–0.55 V vs RHE, $\eta_{cathode}$ = 325 mV) with mesoporous SnO_2 catalysts to a high volume of oxygen vacancy defects.[10] Doping In oxides with Sn as we did may have combined the stabilizing effects of their oxides, leading to the lower onset potentials. These reports and others further prove that In and Sn oxides stabilize CO_2 and improve the selectivity of CO_2RR.[13, 14, 16, 17]

To further investigate the effect of Sn-doping in the ITO catalysts, we performed a Tafel slope analysis for each ligand-stripped catalyst (**See Supplementary Information**). Note that the cathode overpotentials ($\eta_{cathode}$) in **Figure 5** are calculated by using the Nernst equations as follows:

$$\eta_{cathode} = E_{cathode} - (E^{o}_{cathode} - \frac{2.303RT}{zF} log \frac{x_{HCOO^-}}{x_{CO_2}})$$

The common reaction pathway for CO_2 to formate involves a 3-step, 2-electron transfer mechanism:

$$CO_2* + e^- + * \longrightarrow CO_2^{\bullet -}* \quad (1)$$

$$CO_2^{\bullet -}* + H^+ + e^- \longrightarrow HCOO^-* \quad (2)$$

$$HCOO^-* \longrightarrow HCOO^- + * \quad (3)$$

where * and e^- denote an active site and an electron, respectively.[11, 41, 42] As shown in **Figure 5**, the Tafel plots revealed slopes ranging from 27 to 52 mV per decade, with the highest Tafel slope (52 mV per decade) belonging to the undoped In_2O_3 catalyst. From investigating the reaction mechanism for $HCOO^-$, researchers have reported that Tafel slopes of ~59 mV per decade suggest the rate determining step (RDS) to be **Equation 2**, a proton-coupled electron transfer to form $HCOO^-*$;[11, 41] our calculated Tafel slopes align with this conclusion. Typically, the RDS for CO_2 electroreduction, especially to CO and C_2 products, is found to be closer to **Equation 1**, where an electron is transferred to CO_2 [facilitating its adsorption] and the Tafel slope is ~118 mV per decade.[11, 20] A smaller Tafel slope corresponds to better stabilization of the primary reaction intermediates and/or a decrease in the energy barrier for a certain step, therefore signifying that our catalysts stabilize $CO_2^{\bullet -}*$ to a point for further reduction to formate.[42] Sabatier principle studies showed Sn possesses optimal binding strength for *OCHO, a descriptor for $HCOO^-$.[39] The binding strength of Sn promotes $HCOO^-$ formation through the HCOO* pathway

because it is weak enough to allow desorption and discourage poisoning of the Sn catalyst.[43] Since the undoped In_2O_3 catalyst showed the highest Tafel slope, we can conclude that the addition of Sn enhances the stabilization of these intermediates, as stated previously. Yet, we calculated a slightly higher Tafel slope for the 12% ITO catalyst compared to the other Sn-doped samples. This result might be explained by the increased amount of acetate associated with this sample, as another reaction could be occurring along a similar pathway as that for formate production.

Figure 6 shows the XPS analysis of the ITO electrodes before electrolysis testing, with measurements after testing shown in **Figure S7**. The spectra match previously-reported XPS data for undoped In_2O_3 and ITO NCs.[44, 45] Each metal spectrum is fit with two spin-orbit coupled peaks with pseudo-Voigt profiles. These two spin-orbit couples are attributed to the existence of two symmetrically unique metal sites in the material. The XPS survey spectrum shows that the ITO NCs do not contain any impurities (**Figure S8**). The Sn content of each sample was determined by integration of the XPS spectra and compared to the concentration as measured by ICP-AES. The results of this analysis are shown in panel c. Since XPS is a surface-sensitive technique, while ICP-AES is not, the fact that the two concentrations are nearly equal indicates that the Sn is distributed uniformly doped throughout the NC volume. Furthermore, we see no evidence of a change in dopant concentration after CO_2 electrolysis. ICP-AES analysis of the electrolyzer effluent liquids from the undoped In_2O_3 and 6.5% ITO electrode testing shows

no detectable amount of indium or tin ions, which further verifies that the ITO catalysts seem to be stable during the period of the electrolysis experiment.

XRD analysis of the ITO catalysts (specifically undoped In_2O_3 and 5% ITO as representative samples) before and after CO_2 electrolysis was used to assess whether the crystal structure or crystallite size was changed during operation of the electrochemical cell (**Figure 7)**. XRD results indicate that the crystal structure of ITO NC catalysts did not change after CO_2 electrolysis. Scherrer analysis for two of the most intense In_2O_3 diffraction peaks at 30.6 and 35.5 degrees 2Θ indicates the crystallite sizes decreased by ~7% after CO_2 electrolysis (**Table S2**). We also understand that the Sn and In may undergo changes during CO_2 electrolysis, which would ideally require *in situ* characterization techniques (*i.e.*, SERS) to accurately identify.[46-48] Cyclic voltammetry conducted in a 3-electrode cell under both Ar and CO_2 (**Figure S9**) did not reveal any significant surface oxidation or reduction peaks outside of the CO_2RR potential range, suggesting that the Sn and In oxides in the ITO NCs are maintained. In addition, Pourbaix diagrams for Sn and In, which predict oxidation sates based on pH and potential, show that the In and Sn oxides may be stable in alkaline media and under our operating conditions.[49]

Conclusions

The renewable energy-driven electroreduction of CO_2 offers an appealing alternative pathway to

producing carbon fuels and chemicals that are traditionally manufactured using fossil fuels. Formate ($HCOO^-$) is a key chemical for many industries. Heavy post-transition metals such as indium and tin have been identified as promising catalysts for selectively producing $HCOO^-$. While significant efforts have focused on indium, tin, indium oxide, and tin oxide for CO_2 electroreduction, fewer reports have focused on the study of tin-doped indium oxide (ITO) nanocrystals (NCs). Here we investigate the dependence of CO_2 electroreduction efficiency of 20 nm diameter ITO NCs on Sn doping level (0, 1, 5, 6.5, 8, and 12 atomic%). High-quality colloidal ITO NCs with tunable doping concentrations were synthesized using a continuous, controlled growth synthesis. Oleic acid ligands on ITO NC surface sterically stabilize NCs in nonpolar, hydrophobic solvents. However, the presence of such bulky capping molecules also blocks the access of CO_2 reactant molecules to the NC surface, which is disadvantageous for catalytic reactions. To address this issue, we report a ligand-exchange method which enables post-synthetic ligand displacement and phase transfer of colloidal NCs from hexane to water while preserving the NC size and shape. We expect this procedure for base-stripping of X-type ligands could be broadly applicable to additional compositions of colloidal NCs. Employing a flow electrolyzer, we find that ITO NC catalysts exhibit a high selectivity for production of $HCOO^-$ over CO and H_2 (approximately 87% $HCOO^-$, 1-4% CO, and 2-6% H_2 at -0.85 V vs. RHE), an onset potential for $HCOO^-$ as early as -0.21 V vs. RHE, as well as a high partial current density for $HCOO^-$ up to 171 mA/cm^2 at a cathode potential of -1.08 V vs. RHE. The main difference between the catalysts' performances resides in the onset potential

for formate production. Onset of formate production occurred at cell and cathode overpotentials of just -320 mV and -10 mV, respectively, by the 12% ITO. XPS and XRD analysis of the ITO electrodes before and after electrolysis suggest that no or minimal change in surface composition, crystal structure, and particle size of ITO catalysts during CO_2 electrolysis under alkaline conditions. Tafel slope analysis of ITO NC catalysts revealed slopes ranging from 27 to 52 mV per decade, suggesting the rate determining step (RDS) is likely the proton-coupled electron transfer to $CO_2^{\bullet -*}$ to form $HCOO^{-*}$. The low cathode overpotential (~ 10 mV compared to >200 mV typically required) combined with high partial current density and selectivity for $HCOO^-$ observed on ITO NC catalysts suggest doped metal oxide NCs are promising CO_2 reduction catalysts.

Supporting Information

Tafel slope analysis calculations; scanning transmission electron microscopy (STEM) images of as-synthesized ITO NCs at all loadings; size distribution of ligand-stripped and ligand-capped ITO NCs from STEM; titration of ligand-stripped ITO NCs to determine isoelectric point; characterization of undoped In oxide nanocrystals before and after ligand stripping; image of ligand-stripped ITO NCs of each loading dispersed in water; table comparing crystallite size of ligand-stripped and ligand-capped undoped In oxide and 5% ITO NCs using Scherrer analysis; electrode capacitive current measurements using cyclic voltammetry; partial current density and Faradaic efficiency of acetate vs. cathode potential; XPS of ITO

NCs at In 3d and Sn 3d regions after electrolysis; XPS survey spectra of ITO NCs of each loading; table comparing crystallite size of undoped In oxide and 5% ITO NCs before and after electrochemical testing using Scherrer analysis; CV of ITO NCs under Ar and CO_2 in 1 M KOH

Acknowledgments

We gratefully acknowledge financial support by the National Science Foundation through grant CHE-1905263 and the Center for Dynamics and Control of Materials, a National Science Foundation Materials Research Science and Engineering Center (DMR-1720595), and the Welch Foundation (F-1848). We also thank Hsin-Che Lu for helping create some images.

Additional Information

Supplementary information is available in the online version of the paper. Reprints and permissions information is available online. Correspondence and requests for materials should be addressed to P.J.A.Kenis and D.J.Milliron.

Competing Financial Interests

The authors declare no competing financial interests.

Figures

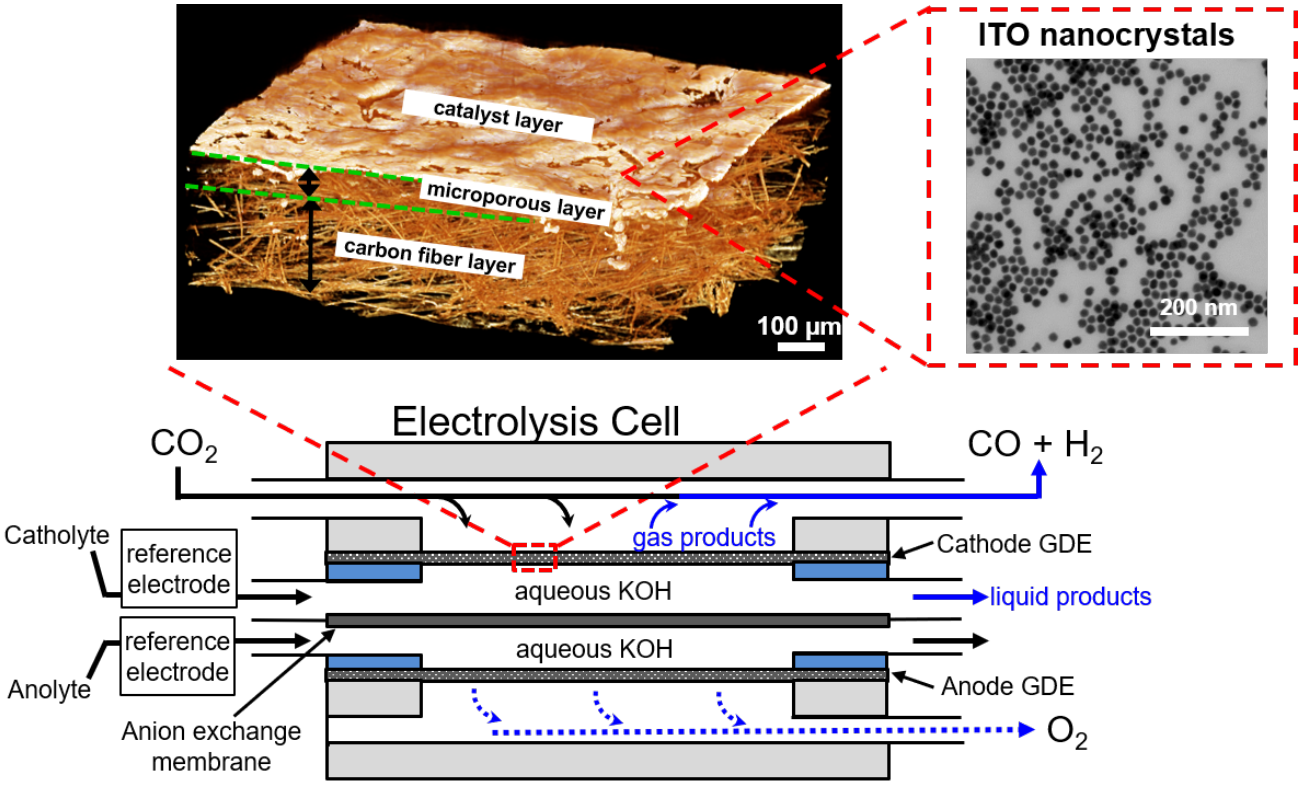

Figure 1. Schematic representation of the microfluidic electrolysis cell (bottom) used in this study for electroreduction of CO_2 to CO and formate. Top-right: STEM of the ITO NC catalyst. Top-left: Reconstructed 3D view (obtained from MicroCT data) of a gas diffusion electrode coated with a 5 at% ligand-stripped ITO catalyst layer (1.0 mg ITO/cm^2), deposited via automated airbrushing.

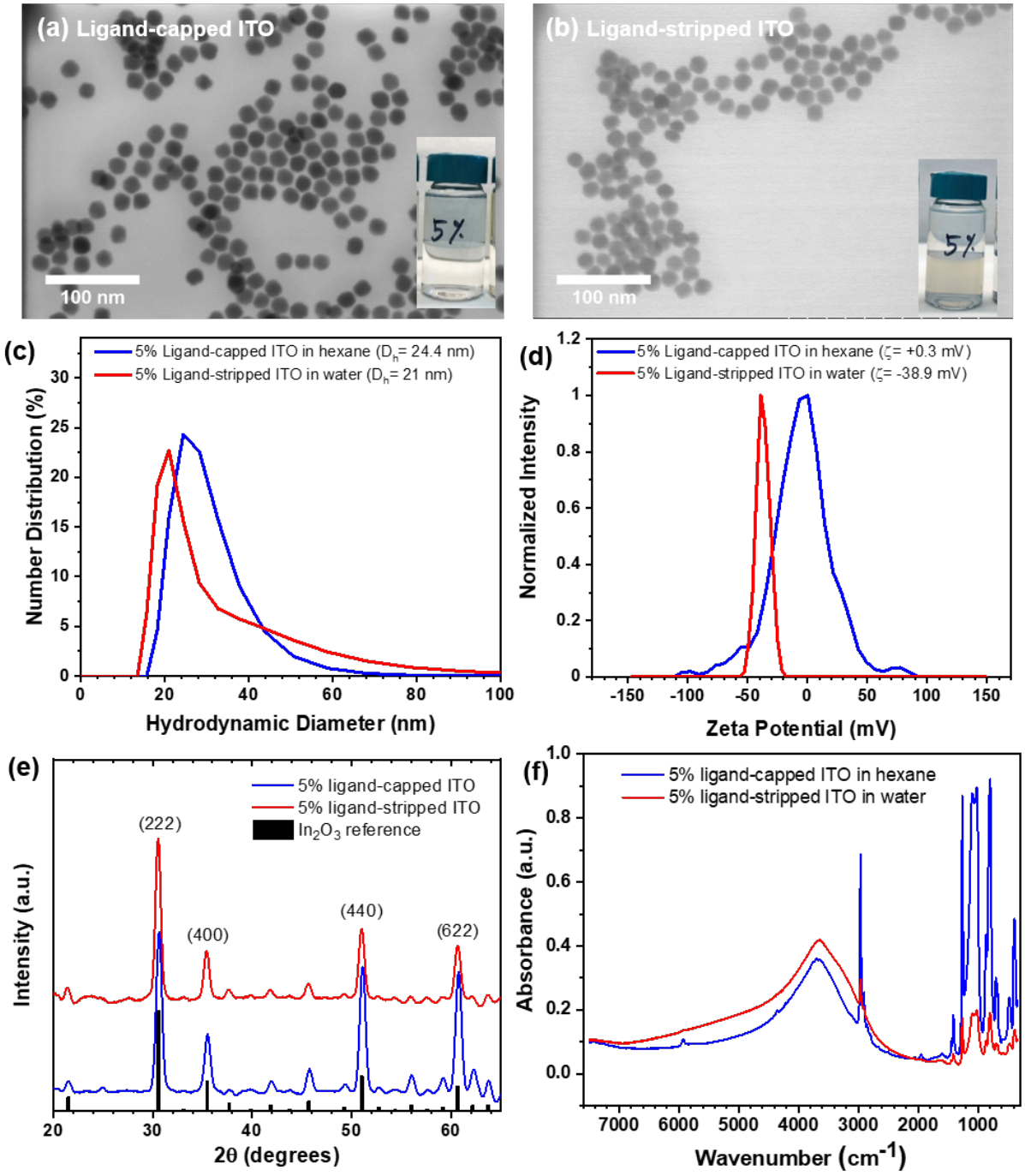

Figure 2. Representative characterization of 20 nm 5 at% ITO NCs before and after KOH ligand stripping treatment. STEM images of ITO (a) before and (b) after ligand stripping, showing unaffected particle size and morphology. (c) DLS measurements of the ligand-capped ITO dispersed in hexane and ligand-stripped ITO dispersed in water, showing the aggregate-free nature of the colloidal dispersion. (d) Zeta potential measurements of ITO before and after ligand stripping, showing surface charge changes from near zero to negative. (e) XRD of ITO, in agreement with In_2O_3 bixbyite reference pattern (PDF

#00-006-0416) at the bottom. (f) FTIR spectra of ITO NCs showing a similar localized surface plasmon peak before and after ligand stripping (broad ~3800 cm^{-1}).

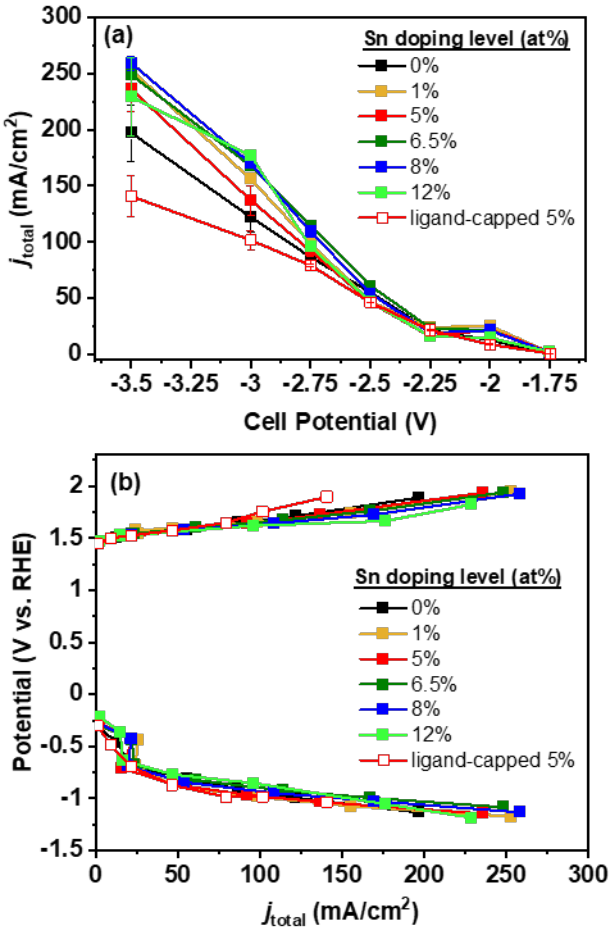

Figure 3. Results of electrochemical reduction of CO_2 using the flow reactor. (a) Current densities as a function of applied cell potential, and (b) corresponding individual electrode polarization curves of the flow reactor operated with ITO catalysts of varying Sn doping levels. Cathode catalyst: 1.0 mg/cm^2 ITO catalysts. Anode catalyst: 1 mg/cm^2 IrO_2 catalyst. Reactant streams: 17 sccm CO_2. Electrolyte: 1.0 M KOH flowing at 0.5 mL/min. Data collected at room temperature and ambient pressure.

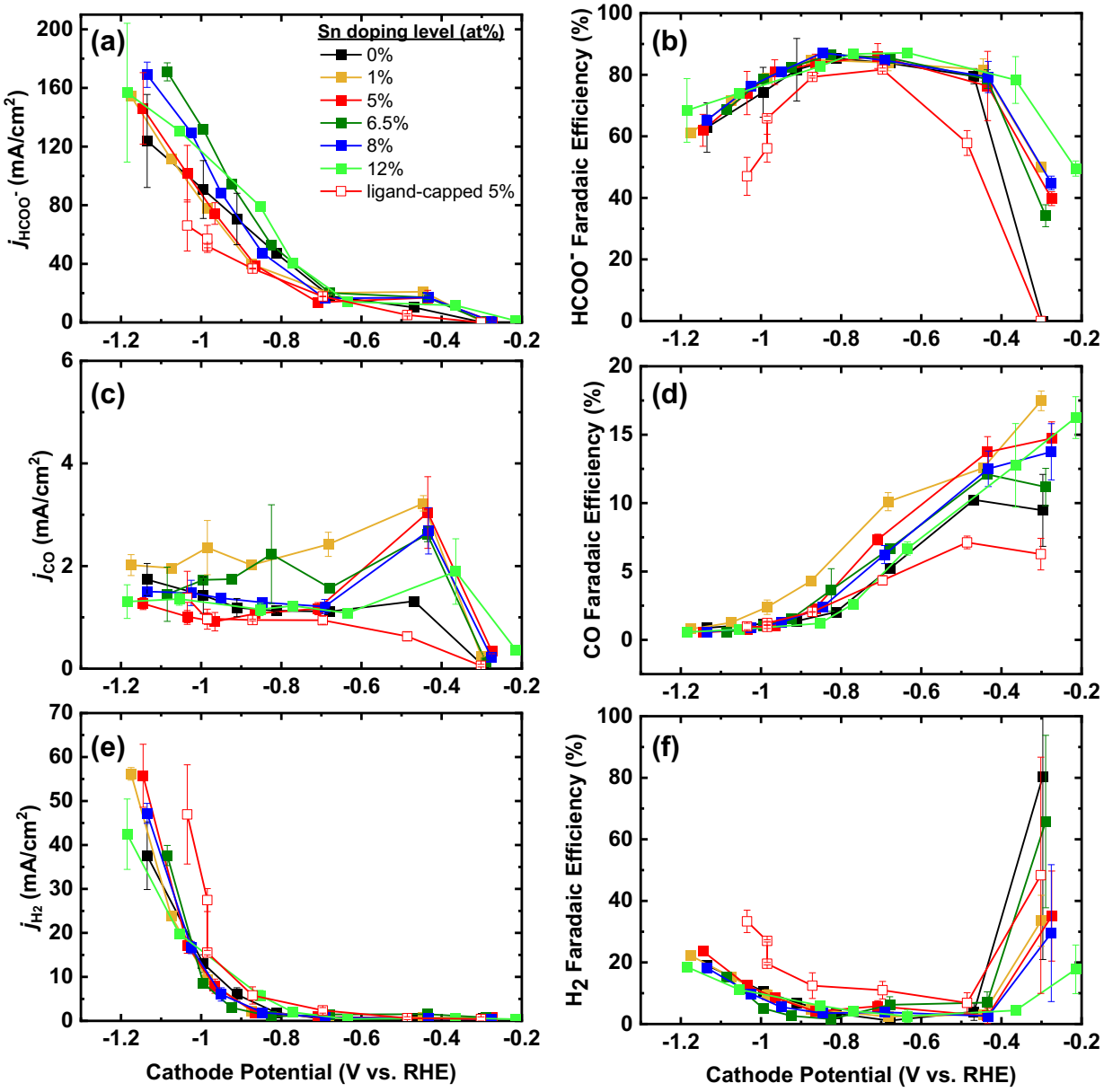

Figure 4. Results of electrochemical reduction of CO_2 using the flow reactor operated with an ITO cathode. Partial current density and Faradaic efficiency for formation of (a,b) formate, (c,d) CO, and (e,f) H_2 as a function of cathode potential (V) vs. RHE. Cathode catalyst: 1.0 mg/cm^2 ITO catalysts. Anode catalyst: 1.0 mg/cm^2 IrO_2. Reactant streams: 17 sccm CO_2. Electrolyte: 1.0 M KOH flowing at 0.5 mL/min. Data collected at room temperature and ambient pressure.

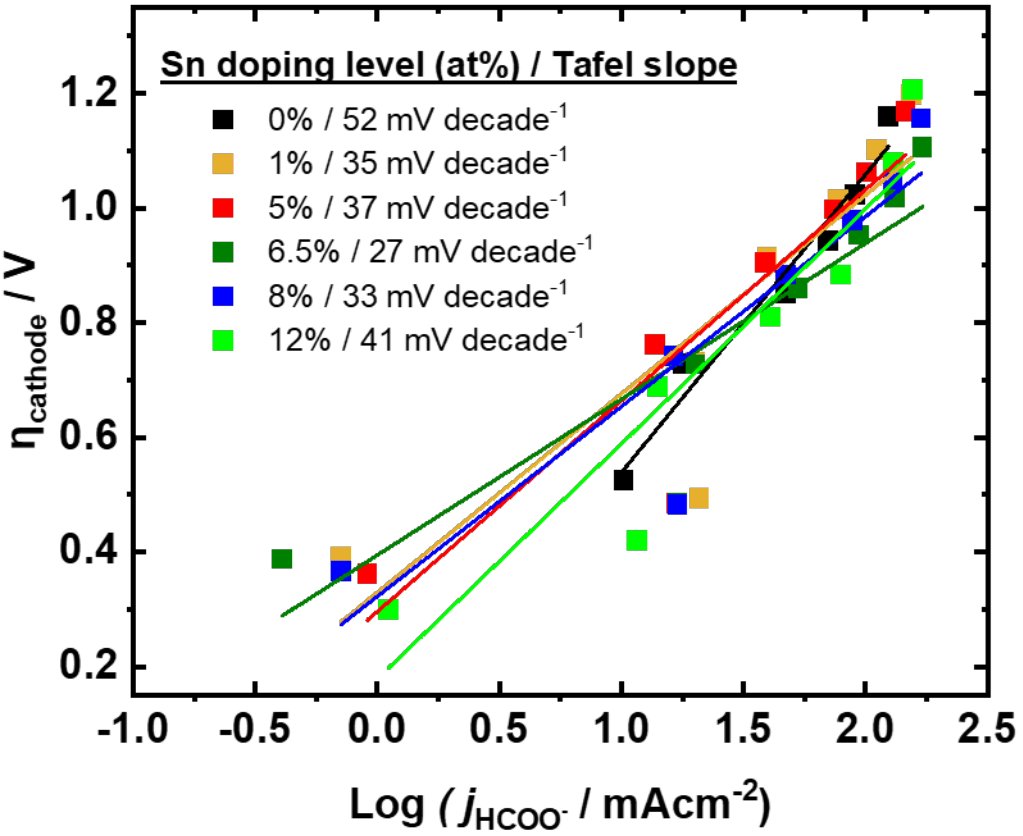

Figure 5. Tafel Slope analysis of ITO catalysts, showing the slopes range from 27-52 mV/decade.

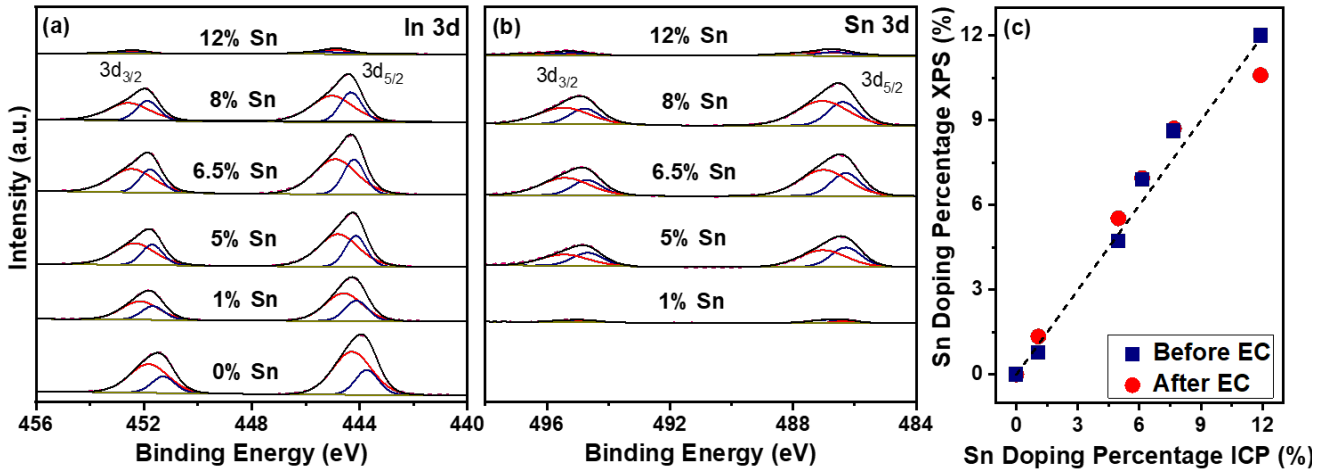

Figure 6. Results of XPS analysis (a) In 3d and (b) Sn 3d electrocatalysts before use. The same for samples after use are provided in Supplementary Information Figure S8. (c) shows the Sn concentration as measured by XPS both before (blue squares) and after (red circles) electrocatalysis as compared to the same measured by ICP, with the 1:1 line shown for reference.

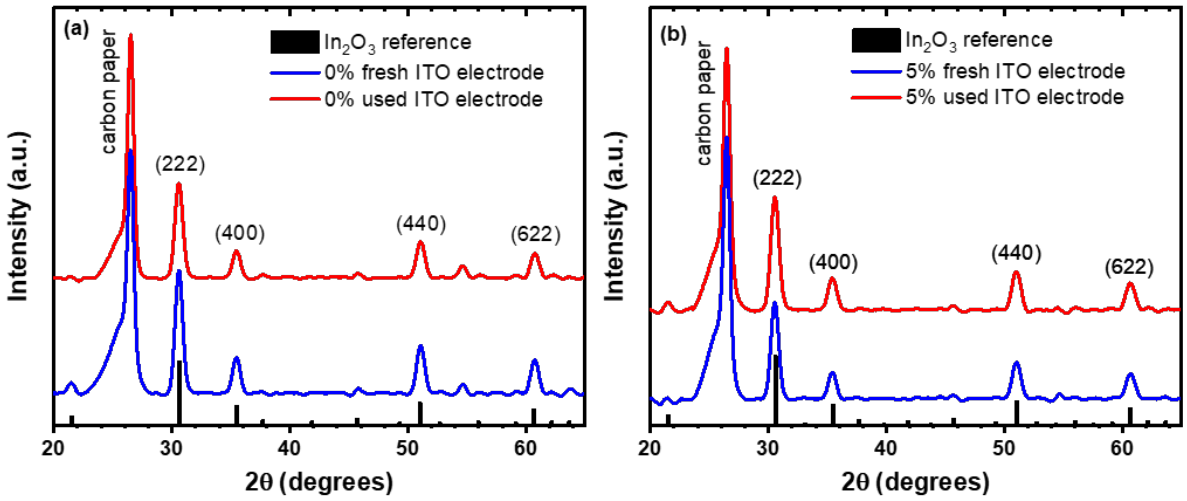

Figure 7. XRD analysis of (a) 0 at% and (b) 5 at% ITO catalyst layer-coated gas diffusion electrodes before and after CO_2 electrolysis, showing stable crystal structure and unaffected particle sizes (Scherrer analysis in Figure S9).

References

1. Davis, S. J.; Caldeira, K.; Matthews, H. D., Future CO_2 Emissions and Climate Change from Existing Energy Infrastructure. *Science* **2010,** 329, (5997), 1330.
2. Chu, S.; Majumdar, A., Opportunities and challenges for a sustainable energy future. *Nature* **2012,** 488, (7411), 294-303.
3. Jhong, H.-R. M.; Ma, S.; Kenis, P. J. A., Electrochemical conversion of CO_2 to useful chemicals: current status, remaining challenges, and future opportunities. *Current Opinion in Chemical Engineering* **2013,** 2, (2), 191-199.
4. Ross, M. B.; De Luna, P.; Li, Y.; Dinh, C.-T.; Kim, D.; Yang, P.; Sargent, E. H., Designing materials for electrochemical carbon dioxide recycling. *Nature Catalysis* **2019,** 2, (8), 648-658.
5. Verma, S.; Lu, S.; Kenis, P. J. A., Co-electrolysis of CO_2 and glycerol as a pathway to carbon chemicals with improved technoeconomics due to low electricity consumption. *Nature Energy* **2019,** 4, (6), 466-474.
6. Hietala, J.; Vuori, A.; Johnsson, P.; Pollari, I.; Reutemann, W.; Kieczka, H., *Formic Acid. In Ullmann's Encyclopedia of Industrial Chemistry, (Ed.)*. **2016**.
7. Detweiler, Z. M.; White, J. L.; Bernasek, S. L.; Bocarsly, A. B., Anodized Indium Metal Electrodes for Enhanced Carbon Dioxide Reduction in Aqueous Electrolyte. *Langmuir* **2014,** 30, (25), 7593-7600.
8. Wang, S.; Wang, J.; Xin, H., Insights into electrochemical CO_2 reduction on tin oxides from first-principles calculations. *Green Energy & Environment* **2017,** 2, (2), 168-171.
9. White, J. L.; Bocarsly, A. B., Enhanced Carbon Dioxide Reduction Activity on Indium-Based Nanoparticles. *J. Electrochem. Soc.* **2016,** 163, (6), H410-H416.
10. Daiyan, R.; Lu, X.; Saputera, W. H.; Ng, Y. H.; Amal, R., Highly Selective Reduction of CO_2 to Formate at Low Overpotentials Achieved by a Mesoporous Tin Oxide Electrocatalyst. *ACS Sustainable Chemistry & Engineering* **2018,** 6, (2), 1670-1679.
11. Chen, Y.; Kanan, M. W., Tin Oxide Dependence of the CO_2 Reduction Efficiency on Tin Electrodes and Enhanced Activity for Tin/Tin Oxide Thin-Film Catalysts. *Journal of the American Chemical Society* **2012,** 134, (4), 1986-1989.
12. Dutta, A.; Kuzume, A.; Kaliginedi, V.; Rahaman, M.; Sinev, I.; Ahmadi, M.; Roldán Cuenya, B.; Vesztergom, S.; Broekmann, P., Probing the chemical state of tin oxide NP catalysts during CO_2 electroreduction: A complementary operando approach. *Nano Energy* **2018,** 53, 828-840.
13. Gu, J.; Héroguel, F.; Luterbacher, J.; Hu, X., Densely Packed, Ultra Small SnO Nanoparticles for Enhanced Activity and Selectivity in Electrochemical CO_2 Reduction. *Angewandte Chemie International Edition* **2018,** 57, (11), 2943-2947.
14. Kumar, B.; Atla, V.; Brian, J. P.; Kumari, S.; Nguyen, T. Q.; Sunkara, M.; Spurgeon, J. M., Reduced SnO_2 Porous Nanowires with a High Density of Grain Boundaries as Catalysts for Efficient Electrochemical CO_2-into-HCOOH Conversion. *Angewandte Chemie International Edition* **2017,** 56,

(13), 3645-3649.
15. Mou, K.; Chen, Z.; Yao, S.; Liu, L., Enhanced electrochemical reduction of carbon dioxide to formate with in-situ grown indium-based catalysts in an aqueous electrolyte. *Electrochimica Acta* **2018,** 289, 65-71.
16. Shaughnessy, C. I.; Jantz, D. T.; Leonard, K. C., Selective electrochemical CO_2 reduction to CO using in situ reduced In2O3 nanocatalysts. *Journal of Materials Chemistry A* **2017,** 5, (43), 22743-22749.
17. Won, D. H.; Choi, C. H.; Chung, J.; Chung, M. W.; Kim, E.-H.; Woo, S. I., Rational Design of a Hierarchical Tin Dendrite Electrode for Efficient Electrochemical Reduction of CO_2. *ChemSusChem* **2015,** 8, (18), 3092-3098.
18. Huang, J.; Buonsanti, R., Colloidal Nanocrystals as Heterogeneous Catalysts for Electrochemical CO_2 Conversion. *Chemistry of Materials* **2019,** 31, (1), 13-25.
19. Ma, S.; Sadakiyo, M.; Luo, R.; Heima, M.; Yamauchi, M.; Kenis, P. J. A., One-step electrosynthesis of ethylene and ethanol from CO_2 in an alkaline electrolyzer. *Journal of Power Sources* **2016,** 301, 219-228.
20. Verma, S.; Hamasaki, Y.; Kim, C.; Huang, W.; Lu, S.; Jhong, H.-R. M.; Gewirth, A. A.; Fujigaya, T.; Nakashima, N.; Kenis, P. J. A., Insights into the Low Overpotential Electroreduction of CO_2 to CO on a Supported Gold Catalyst in an Alkaline Flow Electrolyzer. *ACS Energy Letters* **2018,** 3, (1), 193-198.
21. Staller, C. M.; Gibbs, S. L.; Saez Cabezas, C. A.; Milliron, D. J., Quantitative Analysis of Extinction Coefficients of Tin-Doped Indium Oxide Nanocrystal Ensembles. *Nano Letters* **2019,** 19, (11), 8149-8154.
22. Jansons, A. W.; Hutchison, J. E., Continuous Growth of Metal Oxide Nanocrystals: Enhanced Control of Nanocrystal Size and Radial Dopant Distribution. *ACS Nano* **2016,** 10, (7), 6942-6951.
23. Crockett, B. M.; Jansons, A. W.; Koskela, K. M.; Johnson, D. W.; Hutchison, J. E., Radial Dopant Placement for Tuning Plasmonic Properties in Metal Oxide Nanocrystals. *ACS Nano* **2017,** 11, (8), 7719-7728.
24. Jhong, H.-R. M.; Brushett, F. R.; Kenis, P. J. A., The Effects of Catalyst Layer Deposition Methodology on Electrode Performance. *Advanced Energy Materials* **2013,** 3, (5), 589-599.
25. Buonsanti, R.; Milliron, D. J., Chemistry of Doped Colloidal Nanocrystals. *Chemistry of Materials* **2013,** 25, (8), 1305-1317.
26. Boles, M. A.; Ling, D.; Hyeon, T.; Talapin, D. V., The surface science of nanocrystals. *Nature Materials* **2016,** 15, (2), 141-153.
27. Dong, A.; Ye, X.; Chen, J.; Kang, Y.; Gordon, T.; Kikkawa, J. M.; Murray, C. B., A Generalized Ligand-Exchange Strategy Enabling Sequential Surface Functionalization of Colloidal Nanocrystals. *Journal of the American Chemical Society* **2011,** 133, (4), 998-1006.

28. Jung, S.; McCrory, C. C. L.; Ferrer, I. M.; Peters, J. C.; Jaramillo, T. F., Benchmarking nanoparticulate metal oxide electrocatalysts for the alkaline water oxidation reaction. *Journal of Materials Chemistry A* **2016,** 4, (8), 3068-3076.
29. Wei, C.; Sun, S.; Mandler, D.; Wang, X.; Qiao, S. Z.; Xu, Z. J., Approaches for measuring the surface areas of metal oxide electrocatalysts for determining their intrinsic electrocatalytic activity. *Chemical Society Reviews* **2019,** 48, (9), 2518-2534.
30. Yoon, Y.; Yan, B.; Surendranath, Y., Suppressing Ion Transfer Enables Versatile Measurements of Electrochemical Surface Area for Intrinsic Activity Comparisons. *Journal of the American Chemical Society* **2018,** 140, (7), 2397-2400.
31. Nwabara, U. O.; de Heer, M. P.; Cofell, E. R.; Verma, S.; Negro, E.; Kenis, P. J. A., Towards accelerated durability testing protocols for CO_2 electrolysis. *Journal of Materials Chemistry A* **2020,** 8, (43), 22557-22571.
32. Nwabara, U. O.; Cofell, E. R.; Kenis, P. J. A.; Verma, S.; Negro, E., Durable Cathodes and Electrolyzers for the Efficient Aqueous Electrochemical Reduction of CO_2. *ChemSusChem* **2020,** 13, (5), 855-875.
33. Nwabara, U. O.; Hernandez, A. D.; Henckel, D. A.; Chen, X.; Cofell, E. R.; de-Heer, M. P.; Verma, S.; Gewirth, A. A.; Kenis, P. J. A., Binder-Focused Approaches to Improve the Stability of Cathodes for CO_2 Electroreduction. *ACS Applied Energy Materials* **2021,** 4, (5), 5175-5186.
34. Ma, M.; Clark, E. L.; Therkildsen, K. T.; Dalsgaard, S.; Chorkendorff, I.; Seger, B., Insights into the carbon balance for CO_2 electroreduction on Cu using gas diffusion electrode reactor designs. *Energy & Environmental Science* **2020,** 13, (3), 977-985.
35. Ma, M.; Kim, S.; Chorkendorff, I.; Seger, B., Role of ion-selective membranes in the carbon balance for CO_2 electroreduction via gas diffusion electrode reactor designs. *Chemical Science* **2020,** 11, (33), 8854-8861.
36. Bard, A. J.; Parsons, R.; Jordan, J., Standard potentials in aqueous solution. *New York: M. Dekker, 1985.* **1985**.
37. Verma, S.; Kim, B.; Jhong, H.; Ma, S. C.; Kenis, P. J. A., A Gross-Margin Model for Defining Technoeconomic Benchmarks in the Electroreduction of CO_2. *Chemsuschem* **2016,** 9, (15), 1972-1979.
38. Wang, Y.; Wang, D.; Dares, C. J.; Marquard, S. L.; Sheridan, M. V.; Meyer, T. J., CO_2 reduction to acetate in mixtures of ultrasmall $(Cu)_n$,$(Ag)_m$ bimetallic nanoparticles. *Proceedings of the National Academy of Sciences* **2018,** 115, (2), 278.
39. Feaster, J. T.; Shi, C.; Cave, E. R.; Hatsukade, T.; Abram, D. N.; Kuhl, K. P.; Hahn, C.; Nørskov, J. K.; Jaramillo, T. F., Understanding Selectivity for the Electrochemical Reduction of Carbon Dioxide to Formic Acid and Carbon Monoxide on Metal Electrodes. *ACS Catalysis* **2017,** 7, (7), 4822-4827.
40. Ba, J.; Fattakhova Rohlfing, D.; Feldhoff, A.; Brezesinski, T.; Djerdj, I.; Wark, M.; Niederberger, M., Nonaqueous Synthesis of Uniform Indium Tin Oxide Nanocrystals and Their Electrical

Conductivity in Dependence of the Tin Oxide Concentration. *Chemistry of Materials* **2006,** 18, (12), 2848-2854.
41. Gao, S.; Lin, Y.; Jiao, X.; Sun, Y.; Luo, Q.; Zhang, W.; Li, D.; Yang, J.; Xie, Y., Partially oxidized atomic cobalt layers for carbon dioxide electroreduction to liquid fuel. *Nature* **2016,** 529, (7584), 68-71.
42. Gao, S.; Sun, Z.; Liu, W.; Jiao, X.; Zu, X.; Hu, Q.; Sun, Y.; Yao, T.; Zhang, W.; Wei, S.; Xie, Y., Atomic layer confined vacancies for atomic-level insights into carbon dioxide electroreduction. *Nature Communications* **2017,** 8, (1), 14503.
43. Li, Z.; Cao, A.; Zheng, Q.; Fu, Y.; Wang, T.; Arul, K. T.; Chen, J.-L.; Yang, B.; Adli, N. M.; Lei, L.; Dong, C.-L.; Xiao, J.; Wu, G.; Hou, Y., Elucidation of the Synergistic Effect of Dopants and Vacancies on Promoted Selectivity for CO_2 Electroreduction to Formate. *Advanced Materials* **2021,** 33, (2), 2005113.
44. Staller, C. M.; Robinson, Z. L.; Agrawal, A.; Gibbs, S. L.; Greenberg, B. L.; Lounis, S. D.; Kortshagen, U. R.; Milliron, D. J., Tuning Nanocrystal Surface Depletion by Controlling Dopant Distribution as a Route Toward Enhanced Film Conductivity. *Nano Letters* **2018,** 18, (5), 2870-2878.
45. Wang, T.; Radovanovic, P. V., Size-Dependent Electron Transfer and Trapping in Strongly Luminescent Colloidal Gallium Oxide Nanocrystals. *The Journal of Physical Chemistry C* **2011,** 115, (38), 18473-18478.
46. Chen, X.; Henckel, D. A.; Nwabara, U. O.; Li, Y.; Frenkel, A. I.; Fister, T. T.; Kenis, P. J. A.; Gewirth, A. A., Controlling Speciation during CO_2 Reduction on Cu-Alloy Electrodes. *ACS Catalysis* **2020,** 10, (1), 672-682.
47. Henckel, D. A.; Counihan, M. J.; Holmes, H. E.; Chen, X.; Nwabara, U. O.; Verma, S.; Rodríguez-López, J.; Kenis, P. J. A.; Gewirth, A. A., Potential Dependence of the Local pH in a CO_2 Reduction Electrolyzer. *ACS Catalysis* **2021,** 11, (1), 255-263.
48. Rooney, R. T.; Schmitt, K. G.; von Horsten, H. F.; Schmidt, R.; Gewirth, A. A., Raman and QCM Studies of PPG and PEG Adsorption on Cu Electrode Surfaces. *Journal of The Electrochemical Society* **2018,** 165, (14), D687-D695.
49. Jain, A.; Ong, S. P.; Hautier, G.; Chen, W.; Richards, W. D.; Dacek, S.; Cholia, S.; Gunter, D.; Skinner, D.; Ceder, G.; Persson, K. A., Commentary: The Materials Project: A materials genome approach to accelerating materials innovation. *Apl Mater* **2013,** 1, (1).

TOC Graphic